# Coupled ferroelectricity and superconductivity in bilayer $T_d$-$MoTe_2$

https://doi.org/10.1038/s41586-022-05521-3

Received: 6 June 2022

Accepted: 3 November 2022

Published online: 4 January 2023

Check for updates

Apoorv Jindal[1], Amartyajyoti Saha[2,3], Zizhong Li[4], Takashi Taniguchi[5], Kenji Watanabe[5], James C. Hone[6], Turan Birol[3], Rafael M. Fernandes[2], Cory R. Dean[1], Abhay N. Pasupathy[1]✉ & Daniel A. Rhodes[4]✉

Achieving electrostatic control of quantum phases is at the frontier of condensed matter research. Recent investigations have revealed superconductivity tunable by electrostatic doping in twisted graphene heterostructures and in two-dimensional semimetals such as $WTe_2$ (refs. [1–5]). Some of these systems have a polar crystal structure that gives rise to ferroelectricity, in which the interlayer polarization exhibits bistability driven by external electric fields[6–8]. Here we show that bilayer $T_d$-$MoTe_2$ simultaneously exhibits ferroelectric switching and superconductivity. Notably, a field-driven, first-order superconductor-to-normal transition is observed at its ferroelectric transition. Bilayer $T_d$-$MoTe_2$ also has a maximum in its superconducting transition temperature ($T_c$) as a function of carrier density and temperature, allowing independent control of the superconducting state as a function of both doping and polarization. We find that the maximum $T_c$ is concomitant with compensated electron and hole carrier densities and vanishes when one of the Fermi pockets disappears with doping. We argue that this unusual polarization-sensitive two-dimensional superconductor is driven by an interband pairing interaction associated with nearly nested electron and hole Fermi pockets.

Ferroelectricity has been recently found in a number of two-dimensional (2D) van der Waals layered heterostructures that break inversion symmetry either intrinsically[7,8] or through heterostructure engineering[6]. In contrast to traditional ferroelectricity that arises due to long-range Coulomb interactions in compounds such as $BaTiO_3$ (ref. [9]), this phenomenon is thought to emerge because of the interplay between interlayer sliding and the small dipole moments arising from broken inversion symmetry. For instance, in bilayer hexagonal boron nitride (hBN), out-of-plane electric fields can cause interlayer sliding, changing the stacking order from BA to AB and switching the polarization direction[10]. The same principle has been extended to rhombohedral-stacked bilayer transition metal dichalcogenides[11,12] and orthorhombic-stacked bilayer $T_d$-$WTe_2$ (refs. [7,8]), demonstrating a viable path to achieving ferroelectric behaviour in almost any non-centrosymmetric 2D heterostructure. Compared with thin film oxides (for example, $BiFeO_3$)[13], ferroelectric 2D heterostructures offer compelling advantages: tunable electronic behaviour via conventional electrostatic techniques, modifications through strain and the ability to exploit ferroelectricity to control other electronic states. Importantly, because 2D ferroelectric structures are atomically thin, in-plane metallic states are compatible with the out-of-plane polarization[7]. For example, several metallic transition metal dichalcogenides show 2D superconductivity at low temperatures[14–16]. Ferroelectricity thus offers another tuning knob, in addition to electrostatic doping, to control and assess 2D superconductivity. A possible candidate to achieve this goal is few-layer $T_d$-$MoTe_2$ (hereafter referred to as $MoTe_2$), which has been independently shown to display ferroelectricity and compensated superconductivity[16,17].

In the bulk, $MoTe_2$ is a nearly compensated semimetal[18,19] with a superconducting $T_c$ of 100 mK (refs. [20,21]). Density functional theory (DFT) calculations suggest that monolayer[16] and bilayer $MoTe_2$ (Fig. 1b) retain this charge compensated behaviour, displaying nearly compensated electron and hole pockets at the Fermi level with a small bilayer splitting. The superconducting transition temperature unusually increases with decreasing thickness, reaching a maximum of approximately 7 K in the monolayer limit[16]. This behaviour is distinctly different from other 2D superconductors, in which superconductivity is dominated by a single carrier type, such as monolayer $WTe_2$ (refs. [4,5]) or few-layer $NbSe_2$ (ref. [22]). $MoTe_2$ also takes on a polar crystal structure, where net out-of-plane polarization arises between layers in the few-layer limit. This polarization, along with its out-of-plane switching, has been previously demonstrated via piezoresponse force microscopy measurements[17]. The switching behaviour, similar to that seen in $WTe_2$, has been attributed to interlayer sliding[23,24]. Assuming this to be the case, bilayer $MoTe_2$ is the thinnest possible material that still has the sliding degree of freedom present, and we use it as a platform to study the interaction between the superconducting state and the electric polarization.

For our experiments, we fabricate bilayer $MoTe_2$ samples with dual top and bottom gate electrodes for which the voltages $V_T$ and $V_B$ allow us to tune the carrier density, $\Delta n = \epsilon_{hBN}\epsilon_o(V_T/d_T + V_B/d_B)/e$, and

[1]Department of Physics, Columbia University, New York, NY, USA. [2]School of Physics and Astronomy, University of Minnesota, Minneapolis, MN, USA. [3]Department of Chemical Engineering and Materials Science, University of Minnesota, Minneapolis, MN, USA. [4]Department of Materials Science and Engineering, University of Wisconsin, Madison, WI, USA. [5]National Institute for Materials Science, Tsukuba, Japan. [6]Department of Mechanical Engineering, Columbia University, New York, NY, USA. ✉e-mail: apn2108@columbia.edu; darhodes@wisc.edu

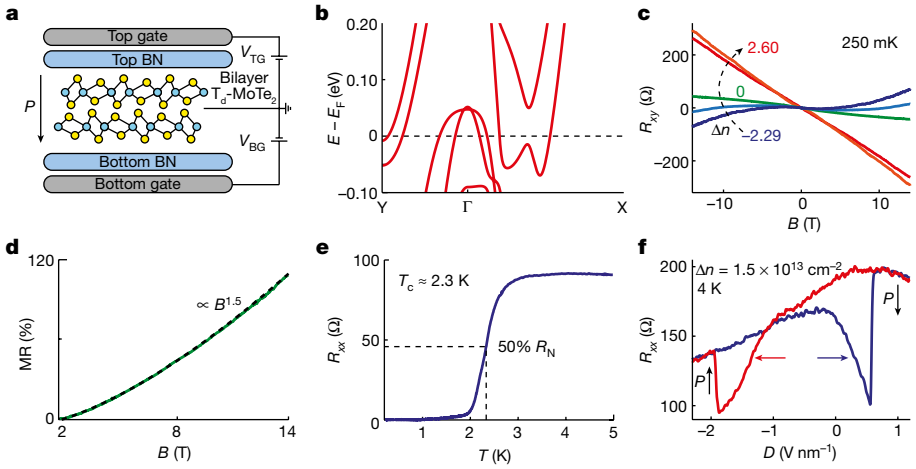


**Fig. 1 | Electronic properties of bilayer $T_d$-$MoTe_2$. a**, Dual-gated device schematic. **P** denotes the direction of internal polarization in the crystal. **b**, DFT calculated electronic band structure for bilayer $MoTe_2$, here $E - E_F$ denotes the relative position of the energy ($E$) with respect to the Fermi level ($E_F$). **c**, Evolution of Hall resistance, $R_{xy}$, with electrostatic doping. $\Delta n$ is in units of $10^{13}$ cm$^{-2}$. **d**, Intrinsic ($\Delta n = 0$) non-saturating magnetoresistance (MR) in bilayer $MoTe_2$; a subquadratic magnetic-field ($B$) dependence is fit to the data (black). **e**, Superconducting transition in bilayer $MoTe_2$ for $\Delta n = 0$. **f**, Ferroelectric switching in bilayer $MoTe_2$ with an applied displacement field.

displacement field, $D = \epsilon_{hBN}(V_T/d_T - V_B/d_B)/2$, independently (Fig. 1a and Supplementary Fig. 2). Here, $d_T$ and $d_B$ are the thickness of top and bottom hBNs, $e$ is the charge of an electron, $\varepsilon_0$ is the vacuum permittivity and $\epsilon_{hBN}$ is the dielectric constant of hBN. Shown in Fig. 1c are measurements of the Hall resistance at 250 mK for several different carrier densities. The data at low $\Delta n$ clearly show that the Hall effect is nonlinear with field. As we increase $\Delta n$, we see the Hall signal evolve from being nonlinear to linear, suggesting a single dominant carrier at high $\Delta n$ (a full discussion of the Hall effect in our device is provided in the Supplementary Information. We also see a non-saturating magnetoresistance at zero doping in our samples, also shown in Fig. 1d. All of these features are hallmarks of compensated semimetals[25–27]. These measurements are, therefore, broadly consistent with the expected electronic structure of pristine material from DFT calculations. This agreement indicates that there is no large external doping or degradation present in our bilayer samples.

Figure 1e shows the resistance of the undoped sample as a function of temperature. A clear superconducting transition is observed, with

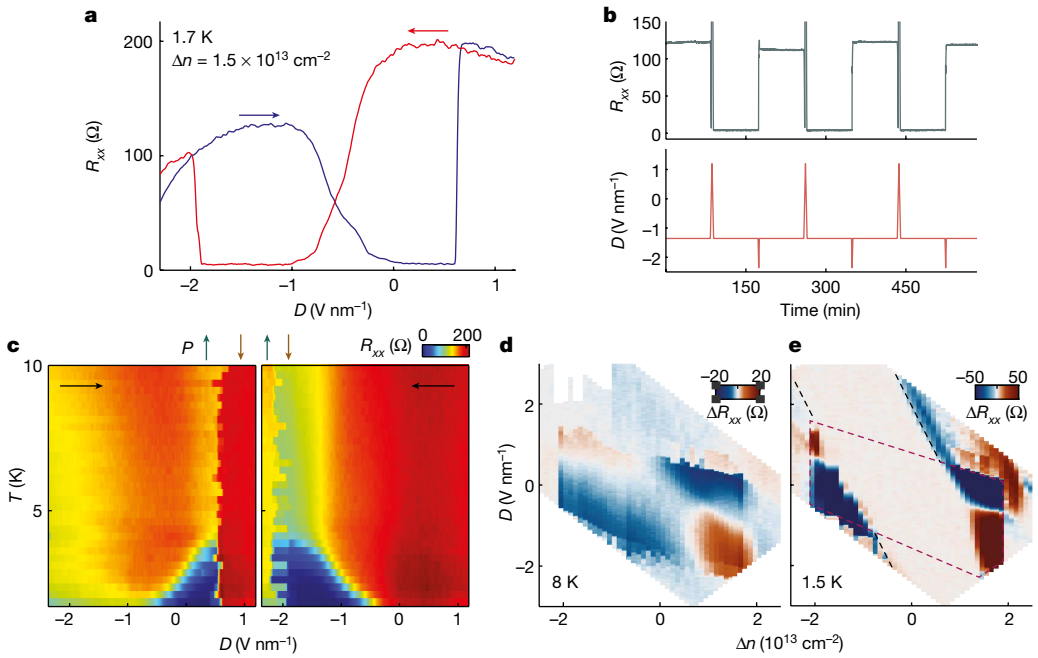


**Fig. 2 | Coupled ferroelectricity and superconductivity in bilayer $T_d$-$MoTe_2$.** **a**, Butterfly loops with bistable normal and superconducting states, indicating coupled ferroelectric and superconducting states. Red and blue arrows denote the direction of the $D$ sweep. **b**, Reversible switching between superconducting and normal states at a fixed charge carrier density as shown in **a**. **c**, Temperature evolution of the coupled ferroelectric and superconducting behaviour at $\Delta n = 1.5 \times 10^{13}$ cm$^{-2}$. A dramatic increase in $T_c$ is observed just before ferroelectric switching. The internal polarization of the crystal is marked with arrows on top. **d**, Resistance difference between displacement field sweep directions shows regions of ferroelectricity at 8 K and its evolution with doping. **e**, At 1.5 K, highlighting the regions of superconductivity. The largest difference in resistance occurs at dopings with hysteretic superconductivity. The magenta dashed line represents the hysteretic region in the normal state. The black dashed line represents the boundary of the field-driven superconductivity.

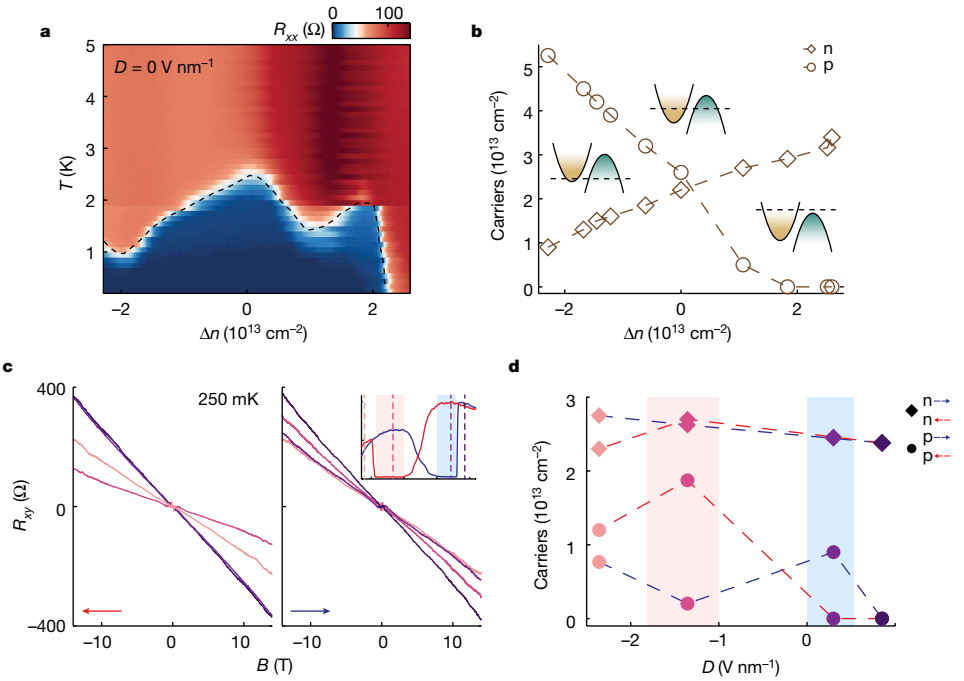


**Fig. 3 | Doping-dependent superconducting properties of bilayer $T_d$-$MoTe_2$.** **a**, Evolution of a superconducting dome with electrostatic doping and temperature. **b**, Carrier concentration as a function of Δ$n$, as extracted by fitting a two-band model to the Hall resistance. **c**, Evolution of Hall resistance at a fixed doping, $\Delta n = 1.5 \times 10^{13}$ cm$^{-2}$, while varying $D$ (inset). **d**, Extracted carrier concentrations from the two-band model to Hall data in **c**. The red and blue dashed lines denote sweeping of $D$ from right to left and left to right, respectively. Diamond and circle colours correspond to their respective Hall response as plotted in **c**.

a $T_c$ of 2.3 K (ref. [16]). To probe the presence of ferroelectricity, we sweep $D$ at a fixed density in the normal state (4 K). We observe hysteretic switching of the four-probe resistance, $R_{xx}$, as shown in Fig. 1f. Although such resistive switching has not previously been observed in $MoTe_2$, it has been seen in multilayered $WTe_2$ (refs. [7,8]). In analogy with $WTe_2$, we associate this resistance bistability with an interlayer sliding transition, which flips the out-of-plane polarization[23,24].

To study how the ferroelectricity interacts with 2D superconductivity at low temperatures, we measure $R_{xx}$ as a function of displacement field at 1.7 K, as shown in Fig. 2a. We clearly observe the presence of both superconductivity and hysteretic switching due to ferroelectricity. Starting from $D < -2$ V nm$^{-1}$ (blue curve, Fig. 2a), both the displacement field and the sample polarization point in the same direction. On decreasing the magnitude of the displacement field and then flipping its sign, superconductivity emerges gradually—resulting in a drop of the sample resistance to zero. The sample remains superconducting until the displacement field switches the crystal's internal polarization, at which point it transitions to the normal state. The behaviour on the downward sweep of displacement field is similar, with the hysteresis expected from the ferroelectricity. The asymmetry of the superconducting butterfly loop with applied field has been seen in other van der Waals ferroelectrics[7,8,10]. Its origin is probably extrinsic to the material itself and is possibly related to substrate and contact asymmetries.

The coexistence of ferroelectric switching and superconductivity in a single material can be used to make a superconducting switch driven by external electric field. We illustrate this in Fig. 2b, which shows the resistance of the sample as a function of time as external fields are applied to the sample. Starting from the normal (superconducting) state, an electric field pulse of appropriate positive (negative) sign can drive a transition to the superconducting (normal) phase. Once the switching between states is established, the resistance of the sample continues to stay in the new state indefinitely, as is seen in the figure. Such a first-order switch for superconductivity may lead to low-temperature classical and quantum electronics applications, such as low-power transistors and tunable qubits in the future.

To explore the connection between ferroelectric switching and superconductivity more carefully, we perform displacement field sweeps at different temperatures, the results of which are summarized in Fig. 2c for the two sweep directions. For the forward direction, as the displacement field is lowered from a high absolute value to a low value, a superconducting transition emerges at low temperatures. On continuing to sweep the displacement field through zero, $T_c$ continues to increase until the displacement field switches the polarization, at which point superconductivity is lost. In both sweep directions, the maximum $T_c$ is therefore seen just before a switching event. This continuous tuning of $T_c$ before switching shows that the mechanism for the superconducting state is intimately tied to the internal electric field of the sample.

The ferroelectric switching behaviour described above is density dependent, as is the observed superconducting behaviour. To understand the region of ferroelectricity in the carrier doping versus displacement field phase diagram, we perform sweeps of the displacement field similar to Fig. 2a at various doping levels, both in the superconducting state and in the normal state. Taking the difference in resistance between the forwards and backwards sweep directions identifies when hysteretic switching is observed in the samples. Shown in Fig. 2d are the results of such measurements in the normal state ($T = 8$ K) and in the superconducting state ($T = 1.5$ K). Focusing on the normal state, we observe that the hysteretic switching in our samples is limited to a doping range of $\Delta n = \pm 2 \times 10^{13}$ cm$^{-2}$ in our measurements. Such a switching behaviour is observed up to 60 K (Supplementary Information). Whether the absence of ferroelectric switching at high doping is an intrinsic effect or whether it is due to constraints of the gate voltages we can achieve in our experiment is currently unclear.

The corresponding measurements in the superconducting state clearly show the role of the internal electric field in the observed superconducting behaviour. In general, we observe that an electric field can drive a superconducting transition in the sample both at low and high

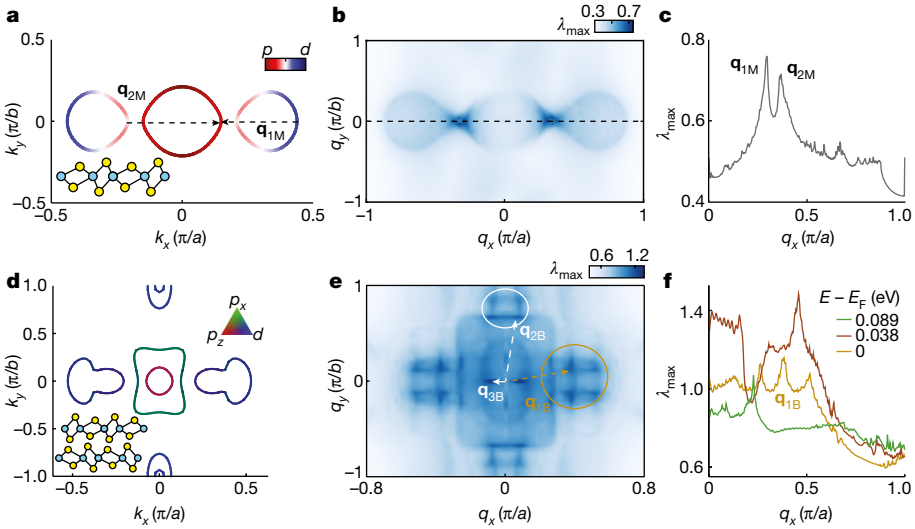


**Fig. 4 | Fermi surface nesting and superconductivity in $MoTe_2$.** **a**, Fermi surface with nesting vectors for monolayer $MoTe_2$, $k_x$, $k_y$, $q_x$ and $q_y$ are wavevectors. Colours of the Fermi surface correspond to orbital projections. **b**, Lindhard susceptibility values, $\lambda_{max}$, for monolayer $MoTe_2$. **c**, Linecut of $\lambda_{max}$ from **b** along the $q_x$ direction with $q_y = 0$. Peaks correspond to interband nesting vectors for electron–hole pockets on the Fermi surface. **d**, The DFT calculated Fermi surface for bilayer $MoTe_2$ showing a hole pocket centred around Γ with electron pockets along the Γ–X and Γ–Y directions. Orbital projections have been depicted in colour with those of the hole pockets being $p_x$ and $p_z$ and that of the electron pocket being $d_{x^2-y^2}$. **e**, $\lambda_{max}$ values for bilayer $MoTe_2$. Local maxima in $\lambda_{max}$ correspond to nesting vectors. $\mathbf{q}_{1B}$ corresponds to the electron–hole nesting vector. **f**, $\lambda_{max}$ as a function of doping. Colours correspond to doping along the band structure as mentioned in the legend.

doping (Fig. 2e, black dashed lines). We see that hysteretic superconductivity occurs in the parts of the phase diagram that are close to the boundary at which field-driven superconductivity intersects with the normal state ferroelectric behaviour. This phenomenology suggests the simple hypothesis that it is the total internal electric field in the sample that controls superconductivity: the sample polarization, when flipped, can turn the superconducting phase on or off if sufficiently close to the field-driven superconducting transition.

So far, we have discussed the displacement-field-dependent properties of the sample. Now, we turn to the carrier-density dependence of superconductivity in the sample at zero displacement field. Shown in Fig. 3a is a colour plot of the temperature-dependent resistance of the sample that shows the presence of a maximum in $T_c$ of 2.5 K. By fitting the Hall measurements in Fig. 1c with a two-band semiclassical model (see the Supplementary Information for details), we extract the independent electron and hole carrier densities of the bilayer (Fig. 3b). This plot shows that the maximum $T_c$ is closely correlated to the compensation point of the material, $\Delta n = 0$. To further confirm our Hall analysis and the compensated behaviour, we measure the magnetoresistance as a function of doping. In agreement with the two-band model, we see a non-saturating magnetoresistance for $\Delta n = 0$ and for intermediate values of $\Delta n$ at which both electron and hole bands cross the Fermi level (Supplementary Information). Upon doping with electrons, we see an overall reduction in $T_c$ until $\Delta n = 2 \times 10^{13}$ cm$^{-2}$ is reached, beyond which superconductivity disappears completely (down to 250 mK). This complete suppression of superconductivity occurs at the same concentration at which the Hall effect becomes linear and the magnetoresistance saturates with increasing magnetic field. Therefore, superconductivity disappears when the chemical potential is raised above the hole pocket. Even though the same trend is seen upon doping with holes, we cannot suppress superconductivity completely as we are limited in the voltage we can safely apply to our gates. The main finding that $T_c$ is maximized near the compensation point is reproduced in multiple devices (Extended Data Fig. 1), but the precise shape of the $T_c$ versus doping curve shows device-to-device variations.

At zero displacement field, it is clear from the discussion above that both hole and electron carriers are required to maximize superconductivity. We can ask whether the same is true when hysteretic superconducting switching is observed. To study this, we measure the Hall effect in the region of ferroelectric hysteresis at $\Delta n = 1.5 \times 10^{13}$ cm$^{-2}$. Shown in Fig. 3c is a subset of these data as the displacement field is swept from right to left (left panel) and from left to right (right panel). The curves are colour-coded for different displacement field values according to the symbols in Fig. 3d. Starting from high positive displacement field, for which the sample is in the normal state, the Hall resistance is linear with field and is well fitted using a single electron band model. As we sweep the field down and enter the superconducting state, the Hall effect develops a pronounced nonlinearity and shows the presence of both types of carriers. Upon switching out of the superconducting state at large negative field, the Hall effect goes back to being nearly linear, showing that the hole carrier density is sharply reduced. The same trend is seen when sweeping the field back from negative to positive values, with a nonlinear Hall effect seen when the sample is superconducting. The extracted carrier concentrations are shown in Fig. 3d, with the hysteretic superconducting regions shaded in red (for the sweep from right to left) and in blue (from left to right). The observation that we need both types of carriers to have superconductivity is clearly seen from this figure.

To further investigate the metallic state from which 2D superconductivity emerges, we measure the temperature dependence of the normal state resistance at various doping levels and zero displacement field, as shown in Extended Data Fig. 2a,b. In bulk $MoTe_2$, the temperature dependence of the resistance is $T^2$ up to 50 K, after which it becomes dominated by phonon scattering[28]. On the other hand, for bilayer $MoTe_2$, we observe an approximately linear-in-$T$ resistance for intermediate temperatures. For most doping values, the resistance recovers the usual $T^2$ dependence at low temperatures, as shown in Extended Data Fig. 2c. However, as summarized in Extended Data Fig. 2c, for a narrow range of $\Delta n$ near the edge of the superconducting dome, the $T$-linear behaviour persists down to the superconducting $T_c$. This behaviour has been qualitatively reproduced in at least one other device (Extended Data Fig. 3). In certain unconventional superconductors[29,30] and other 2D correlated systems[31,32], a $T$-linear resistance is often associated with an underlying strange metallic state, the origin

of which remains widely debated. In the present case of bilayer $MoTe_2$, it is important to notice that the $T$-linear contribution is comparable with the residual resistance.

The fact that superconductivity appears only when both electron and hole pockets are present suggests that interband processes are behind the pairing mechanism. The situation is reminiscent of iron-pnictide superconductors, which are also compensated semimetals[33]. In that case, it has been proposed that the pairing interaction is enhanced by spin fluctuations. Interestingly, previous results on monolayer $MoTe_2$ have hypothesized that the enhancement in $T_c$ was unconventional and probably related to enhanced spin fluctuations[16]. To further analyse this scenario, we compute the leading eigenvalue $\lambda_{max}$ of the multi-orbital Lindhard susceptibility from DFT calculations (see Methods for details). To set the stage, we first consider the monolayer case, the Fermi surface of which is shown in Fig. 4a. As seen in Fig. 4b,c, $\lambda_{max}$ peaks at the two nesting wavevectors $\mathbf{q}_{1M}$ and $\mathbf{q}_{2M}$ (M = monolayer) that connect the edges of the electron and hole pockets along the $k_x$ axis.

The situation in bilayer $MoTe_2$ is slightly more complicated because of the presence of an additional electron pocket along the $k_y$ direction as well as the bilayer splitting (Fig. 4d). As a result, $\lambda_{max}$ displays a peak not only at the nesting wavevector $\mathbf{q}_{1B}$ (B = bilayer), connecting the hole and electron pockets approximately along $k_x$, but also at the wavevector $\mathbf{q}_{2B}$, connecting the hole and electron pockets along $k_y$ (Fig. 4e). Moreover, an additional peak appears at $\mathbf{q}_{3B}$, which connects the bilayer-split hole pockets. Electron–electron interactions involving the same or different orbitals are expected to enhance one or more of these peaks, thus providing a possible mechanism for the interband pairing interaction. This would imply that $MoTe_2$ is a rather unusual 2D superconductor. Although other mechanisms cannot be ruled out at present, this simple nesting-driven scenario is qualitatively consistent with the doping dependence of $T_c$ observed in bilayer $MoTe_2$. Indeed, as shown in Fig. 4f, the peak of $\lambda_{max}$ at $\mathbf{q}_{1B}$ first increases for small electron doping and then decreases and disappears once the hole pocket is pushed down below the Fermi level.

Our finding of a tunable $T_c$ in the ferroelectric regime of bilayer $MoTe_2$ shows that this material is a promising platform for controlling an unusual type of 2D superconductivity with two independent and highly precise knobs: doping and displacement field. At the same time, the discrete switching of superconductivity at the ferroelectric transition opens up new possibilities for quantum devices with a first-order switch for the superconducting phase. We expect that these effects will have an interesting dependence on layer thickness[8] and twist angle that tunes the degree of inversion symmetry breaking[10]. Such effects should also be present in other non-centrosymmetric 2D superconductors[34]. Finally, the control of these properties using ultrafast electromagnetic excitations that couple to the lattice is also an appealing prospect[35,36].

## Online content

Any methods, additional references, Nature Portfolio reporting summaries, source data, extended data, supplementary information, acknowledgements, peer review information; details of author contributions and competing interests; and statements of data and code availability are available at https://doi.org/10.1038/s41586-022-05521-3.


1. Cao, Y. et al. Unconventional superconductivity in magic-angle graphene superlattices. *Nature* **556**, 43–50 (2018).
2. Liu, X. et al. Tunable spin-polarized correlated states in twisted double bilayer graphene. *Nature* **583**, 221–225 (2020).
3. Park, J. M., Cao, Y., Watanabe, K., Taniguchi, T. & Jarillo-Herrero, P. Tunable strongly coupled superconductivity in magic-angle twisted trilayer graphene. *Nature* **590**, 249–255 (2021).
4. Fatemi, V. et al. Electrically tunable low-density superconductivity in a monolayer topological insulator. *Science* **362**, 926–929 (2018).
5. Sajadi, E. et al. Gate-induced superconductivity in a monolayer topological insulator. *Science* **362**, 922–925 (2018).
6. Zheng, Z. et al. Unconventional ferroelectricity in moiré heterostructures. *Nature* **588**, 71–76 (2020).
7. De la Barrera, S. C. et al. Direct measurement of ferroelectric polarization in a tunable semimetal. *Nat. Commun.* **12**, 5298 (2021).
8. Fei, Z. et al. Ferroelectric switching of a two-dimensional metal. *Nature* **560**, 336–339 (2018).
9. Rabe, K. M., Dawber, M., Lichtensteiger, C., Ahn, C. H. & Triscone, J.-M. in *Physics of Ferroelectrics* 1–30 (Springer, 2007).
10. Yasuda, K., Wang, X., Watanabe, K., Taniguchi, T. & Jarillo-Herrero, P. Stacking-engineered ferroelectricity in bilayer boron nitride. *Science* **372**, 1458–1462 (2021).
11. Wang, X. et al. Interfacial ferroelectricity in rhombohedral-stacked bilayer transition metal dichalcogenides. *Nat. Nanotechnol.* **17**, 367–371 (2022).
12. Liu, Y., Liu, S., Li, B., Yoo, W. J. & Hone, J. Identifying the transition order in an artificial ferroelectric van der Waals heterostructure. *Nano Lett.* **22**, 1265–1269 (2022).
13. Sando, D., Barthélémy, A. & Bibes, M. $BiFeO_3$ epitaxial thin films and devices: past, present and future. *J. Phys. Condens. Matter* **26**, 473201 (2014).
14. Ye, J. et al. Liquid-gated interface superconductivity on an atomically flat film. *Nat. Mater.* **9**, 125–128 (2010).
15. Hamill, A. et al. Two-fold symmetric superconductivity in few-layer NbSe2. *Nat. Phys.* **17**, 949–954 (2021).
16. Rhodes, D. A. et al. Enhanced superconductivity in monolayer Td-$MoTe_2$. *Nano Lett.* **21**, 2505–2511 (2021).
17. Yuan, S. et al. Room-temperature ferroelectricity in $MoTe_2$ down to the atomic monolayer limit. *Nat. Commun.* **10**, 1775 (2019).
18. Deng, K. et al. Experimental observation of topological Fermi arcs in type-IIWeyl semimetal $MoTe_2$. *Nat. Phys.* **12**, 1105–1110 (2016).
19. Jiang, J. et al. Signature of type-II Weyl semimetal phase in $MoTe_2$. *Nat. Commun.* **8**, 13973 (2017).
20. Qi, Y. et al. Superconductivity in Weyl semimetal candidate $MoTe_2$. *Nat. Commun.* **7**, 11038 (2016).
21. Wang, W. et al. Evidence for an edge supercurrent in the Weyl superconductor $MoTe_2$. *Science* **368**, 534–537 (2020).
22. Xi, X. et al. Ising pairing in superconducting NbSe2 atomic layers. *Nat. Phys.* **12**, 139–143 (2016).
23. Yang, Q., Wu, M. & Li, J. Origin of two-dimensional vertical ferroelectricity in $WTe_2$ bilayer and multilayer. *J. Phys. Chem. Lett.* **9**, 7160–7164 (2018).
24. Liu, X. et al. Vertical ferroelectric switching by in-plane sliding of two-dimensional bilayer $WTe_2$. *Nanoscale* **11**, 18575–18581 (2019).
25. Sondheimer, E. & Wilson, A. H. The theory of the magneto-resistance effects in metals. *Proc. R. Soc. Lond. A* **190**, 435–455 (1947).
26. Chen, F. et al. Extremely large magnetoresistance in the type-II Weyl semimetal $MoTe_2$. *Phys. Rev. B* **94**, 235154 (2016).
27. Ali, M. N. et al. Large, non-saturating magnetoresistance in $WTe_2$. *Nature* **514**, 205–208 (2014).
28. Zandt, T., Dwelk, H., Janowitz, C. & Manzke, R. Quadratic temperature dependence up to 50 K of the resistivity of metallic $MoTe_2$. *J. Alloys Compd* **442**, 216–218 (2007).
29. Hussey, N., Buhot, J. & Licciardello, S. A tale of two metals: contrasting criticalities in the pnictides and hole-doped cuprates. *Rep. Progr. Phys.* **81**, 052501 (2018).
30. Greene, R. L., Mandal, P. R., Poniatowski, N. R. & Sarkar, T. The strange metal state of the electron-doped cuprates. *Ann. Rev. Condens. Matter Phys.* **11**, 213–229 (2020).
31. Cao, Y. et al. Strange metal in magic-angle graphene with near Planckian dissipation. *Phys. Rev. Lett.* **124**, 076801 (2020).
32. Ghiotto, A. et al. Quantum criticality in twisted transition metal dichalcogenides. *Nature* **597**, 345–349 (2021).
33. Fernandes, R. M. et al. Iron pnictides and chalcogenides: a new paradigm for superconductivity. *Nature* **601**, 35–44 (2022).
34. Zhai, B., Li, B., Wen, Y., Wu, F. & He, J. Prediction of ferroelectric superconductors with reversible superconducting diode effect. *Phys. Rev. B* **106**, L140505 (2022).
35. Li, X. et al. Terahertz field-induced ferroelectricity in quantum paraelectric $SrTiO_3$. *Science* **364**, 1079–1082 (2019).
36. Ji, S., Granas, O. & Weissenrieder, J. Manipulation of stacking order in $T_d$-$WTe_2$ by ultrafast optical excitation. *ACS Nano* **15**, 8826–8835 (2021).

# Methods

### Crystal growth

Single crystals were grown by a self-flux method using excess Te. Mo powder, 99.9975%, was loaded into a Canfield crucible with Te, 99.9999% lump in a ratio of 1:25 (Mo:Te) and subsequently sealed in a quartz ampoule under vacuum (around 1 mTorr). Afterwards, the ampoule was heated to 1,120 °C over 12 h, and then held at this temperature for 2 days before cooling down to 880 °C over a period of 3 weeks; it was then subsequently centrifuged to remove excess Te. After removing crystals from the original quartz ampoule, crystals were again resealed under vacuum in a quartz ampoule and annealed in a temperature gradient with the crystals held at the hot end at 435 °C and the cold end of the ampoule held at room temperature for 2 days. The final annealing rids the crystals of any interstitial Te and is critical for obtaining the highest residual resistivity ratios.

### Device fabrication

Few-layered $MoTe_2$ is extremely air sensitive and degrades within a matter of minutes under ambient conditions[37]. Therefore, bilayer $T_d$-$MoTe_2$ devices were fabricated in a nitrogen-filled glovebox with $H_2O$ and $O_2$ levels below 0.5 ppm and electrical contact made using prepatterned electrodes fully encapsulated in hBN (top hBN layer thickness, 29 nm; bottom hBN layer thickness, 7 nm) on a metal backgate. First, local backgates were defined on $Si/SiO_2$ substrates using traditional e-beam lithography (EBL) techniques, with metal deposited using e-beam deposition (2/10 nm Ti/Pd) and then cleaned via ultrahigh vacuum annealing at 300 °C with subsequent exposure to a low-power $O_2$ plasma for 10 min. Thin hBN (7–10 nm thickness) was dry transferred using either polypropylene carbonate or poly(bisphenol A carbonate) on to the metal backgates. This was followed with another EBL step, to define the prepatterned contacts that did not extend beyond the hBN edge, and e-beam deposition (2/12 nm Ti/AuPd). Prepatterned contacts were then cleaned using an atomic force microscope tip in contact mode (force ≈ 300 nN, tip radius 7 nm) and loaded into a nitrogen or argon-filled glovebox. Few-layer $MoTe_2$ was mechanically exfoliated onto a polydimethylsiloxane stamp and then transferred onto $Si/SiO_2$ substrates. Bilayers were then identified via optical contrast on the $Si/SiO_2$ substrates, and later confirmed by measuring $R_{xx}$ and, where possible, step height using an atomic force microscope. To complete the heterostructure, hBN (20–30 nm thickness) was then picked up via a dry stacking method[38] using polypropylene carbonate as the polymer. The picked-up hBN was then used to pickup bilayer $MoTe_2$ and the hBN/$MoTe_2$ stack was subsequently transferred on to the bottom hBN/prepatterns at 120 °C. Afterwards, through holes were defined in a polymethyl methacrylate resist (950k A6), and etched using EBL and reactive ion etching with $SF_6/O_2$ plasma. A final EBL and e-beam deposition step was used to define and deposit a top gate and contacts on the prepatterns (2/30/90 nm Ti/Pd/Au).

### Electrical transport

Electrical transport measurements of our devices were performed either in a $^3$He cryostat equipped with a superconducting magnet (14 T) or in a $^4$He variable temperature insert with a base temperature of 1.7 K. Standard lock-in measurements were taken with an a.c. excitation (37.77 Hz) of 10–100 nA using an SR860 or SR830 lock-in amplifier with a 1 MΩ resistor in series ($V_{bias}$ = 10–100 mV). For measurements pertaining to superconductivity, passive resistor–capacitor (RC) filters with a cutoff frequency of approximately 50 kHz, which were kept at around 4 K near the sample space, were used on both current and voltage contacts.

### Theoretical calculations

First-principles DFT calculations were performed with the projector augmented wave formalism as implemented in the Vienna ab initio simulation package[39–42]. The PBEsol exchange correlation functional[43] was used with a 360 eV cutoff energy for the plane-wave basis. The in-plane lattice parameters for monolayer and bilayer $MoTe_2$ structures were fixed to $a$ = 6.33 Å and $b$ = 3.469 Å, obtained experimentally from the bulk structure[44], and the internal ionic coordinates were relaxed. A shifted Monkhorst–Pack grid[45] of 9 × 18 × 3$k$ points was used for the monolayer and a grid of 8 × 16 × 2$k$ points was used for the bilayer primitive cell. Spin–orbit coupling was not included as we found that it did not generate significant qualitative differences in the Fermi surface. The WANNIER90 package[46,47] was used to calculate maximally localized Wannier functions. From these, a four-band tight-binding model was obtained for the monolayer, with 2,736 in-plane nearest-neighbour hopping parameters involving the $p_x$ and $d$ orbitals of the two inequivalent Te and Mo atoms, respectively, in the unit cell. Note that not all hopping parameters are independent owing to symmetry constraints. A ten-band tight-binding model was constructed for the bilayer, with two $p_z$ orbitals added to account for the interlayer interaction, resulting in 15,300 in-plane nearest-neighbour hopping parameters. The static multi-orbital Lindhard susceptibility tensor $\chi^{\alpha\beta\gamma\delta}(\mathbf{q})$ was defined according to[48]:

$$\chi^{\alpha\beta}_{\gamma\delta}(\mathbf{q}) = -\frac{1}{N}\sum_{\mathbf{k},mn}\frac{a^{\gamma}_{m}(\mathbf{k})a^{\alpha *}_{m}(\mathbf{k})a^{\beta}_{n}(\mathbf{k}+\mathbf{q})a^{\delta *}_{n}(\mathbf{k}+\mathbf{q})}{E_n(\mathbf{k}+\mathbf{q})-E_m(\mathbf{k})+i0^{+}}\left[f(E_n(\mathbf{k}+\mathbf{q}))-f(E_m(\mathbf{k}))\right] \quad (1)$$

where $a^{\gamma}_{m}(\mathbf{k})$ are eigenvector components associated with the change from the orbital basis (Greek letters) to the band basis (Latin letters), $E_m(\mathbf{k})$ are the energy eigenvalues in the band basis and $f(E)$ is the Fermi function, which at $T$ = 0 becomes the theta function $\theta(E - E_F)$. The eigenvalue problem[49] $\chi^{\alpha\beta\gamma\delta}v^{(n)}_{\alpha\beta} = \lambda^{(n)}v^{(n)}_{\gamma\delta}$ was then solved to find the maximum eigenvalue $\lambda_{max} \equiv \max(\lambda^{(n)})$ for each momentum value with PythTB[50] and in-house scripts, using a 50 × 100 grid for the internal momentum sum.

## Data availability

Datasets used to construct plots and support other findings in this article are available from the corresponding authors upon request.


37. Gan, Y. et al. Bandgap opening in $MoTe_2$ thin flakes induced by surface oxidation. *Front. Phys.* **15**, 33602 (2020).
38. Wang, L. et al. One-dimensional electrical contact to a two-dimensional material. *Science* **342**, 614–617 (2013).
39. Kresse, G. & Furthmüller, J. Efficiency of ab-initio total energy calculations for metals and semiconductors using a plane-wave basis set. *Comput. Mater. Sci.* **6**, 15–50 (1996).
40. Kresse, G. & Furthmüller, J. Efficient iterative schemes for ab initio total-energy calculations using a plane-wave basis set. *Phys. Rev. B* **54**, 11169 (1996).
41. Blöchl, P. E. Projector augmented-wave method. *Phys. Rev. B* **50**, 17953 (1994).
42. Kresse, G. & Joubert, D. From ultrasoft pseudopotentials to the projector augmented-wave method. *Phys. Rev. B* **59**, 1758 (1999).
43. Perdew, J. P. et al. Restoring the density-gradient expansion for exchange in solids and surfaces. *Phys. Rev. Lett.* **100**, 136406 (2008).
44. Brown, B. E. The crystal structures of $WTe_2$ and high-temperature $MoTe_2$. *Acta Crystallogr.* **20**, 268–274 (1966).
45. Monkhorst, H. J. & Pack, J. D. Special points for Brillouin-zone integrations. *Phys. Rev. B* **13**, 5188 (1976).
46. Mostofi, A. A. et al. wannier90: A tool for obtaining maximally-localised Wannier functions. *Comput. Phys. Commun.* **178**, 685–699 (2008).
47. Marzari, N., Mostofi, A. A., Yates, J. R., Souza, I. & Vanderbilt, D. Maximally localized Wannier functions: theory and applications. *Rev. Mod. Phys.* **84**, 1419 (2012).
48. Graser, S., Maier, T., Hirschfeld, P. & Scalapino, D. Near-degeneracy of several pairing channels in multiorbital models for the Fe pnictides. *N. J. Phys.* **11**, 025016 (2009).
49. Christensen, M. H., Kang, J., Andersen, B. M. & Fernandes, R. M. Spin-driven nematic instability of the multiorbital Hubbard model: Application to iron-based superconductors. *Phys. Rev. B* **93**, 085136 (2016).
50. Python Tight Binding (PythTB) (2021); http://physics.rutgers.edu/pythtb/



**Acknowledgements** We thank A. Millis for discussions. The experimental portion of this research was primarily supported by the NSF MRSEC program through Columbia University in the Center for Precision-Assembled Quantum Materials under award no. DMR-2011738

(fabrication, measurements and data analysis). A.S., T.B. and R.M.F. (theoretical modelling) were supported by the National Science Foundation through the University of Minnesota MRSEC (grant no. DMR-2011401). D.A.R. and Z.L. (growth, measurements and data analysis) were supported by the University of Wisconsin-Madison, Office of the Vice Chancellor for Research and Graduate Education with funding from the Wisconsin Alumni Research Foundation. D.A.R. was partially supported by the NSF MRSEC program through the University of Wisconsin-Madison under award no. DMR-1720415. A.N.P. acknowledges salary support from the NSF via grant no. DMR-2004691, from AFOSR via grant no. FA9550-21-1-0378 by the ARO-MURI program with award no. W911NF-21-1-0327. K.W. and T.T. acknowledge support from the Element Strategy Initiative conducted by the MEXT, Japan (grant no. JPMXP0112101001) and JSPS KAKENHI (grant nos. 19H05790, 20H00354 and 21H05233).

**Author contributions** The experiment was designed by D.A.R., A.J. and A.N.P. Devices were fabricated by A.J., D.A.R. and Z.L. C.R.D., A.J. and D.A.R. performed the measurements and analysed the data. A.S. developed theoretical models and performed calculations supervised by T.B. and R.F.M. T.T. and K.W. supplied hBN single crystals. D.A.R. and J.C.H. synthesized $MoTe_2$ single crystals. D.A.R., A.J. and A.N.P. wrote the manuscript with the input of all other authors.

**Competing interests** The authors declare no competing interests.

**Additional information**

**Supplementary information** The online version contains supplementary material available at https://doi.org/10.1038/s41586-022-05521-3.

**Correspondence and requests for materials** should be addressed to Abhay N. Pasupathy or Daniel A. Rhodes.

**Peer review information** *Nature* thanks Yoichi Yanase, Kenji Yasuda and the other, anonymous, reviewer(s) for their contribution to the peer review of this work. Peer reviewer reports are available.

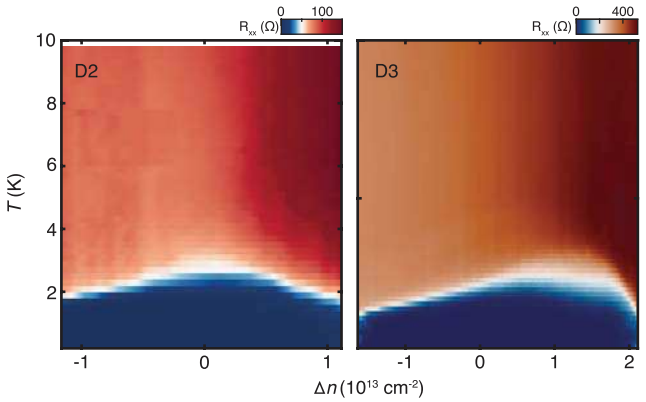


**Extended Data Fig. 1 | Superconducting dome observed in two other devices at D = 0 V/nm.** Limitations due to the dielectric strength of the *h*BN in these devices precluded us from reaching higher doping and, consequently, the formation of a complete superconducting dome.

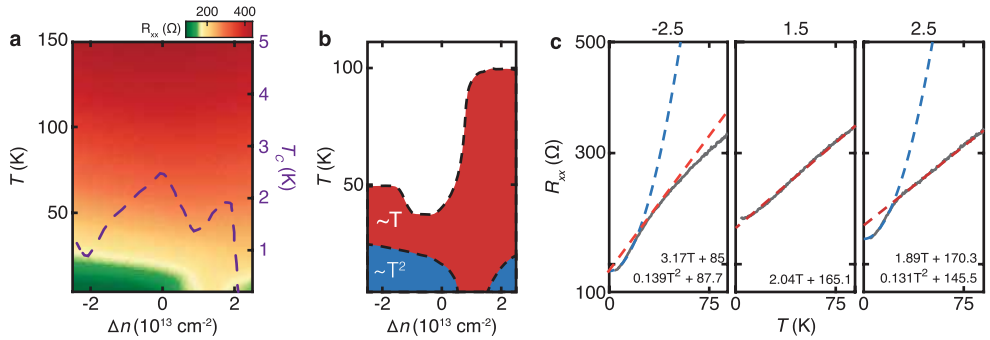


**Extended Data Fig. 2 | Doping dependent T-linear behaviour of bilayer $T_d$-$MoTe_2$. a**, Colour plot of resistance vs temperature and doping. Doping dependent superconducting critical temperature (from Fig. 3a) is superimposed on the colour plot with the associated temperature scale on the right axis. **b**, Diagram indicating regions of $T^2$ and $T$-linear behaviour. **c**, $R_{xx}$ versus temperature for various dopings, as indicated at the top of each curve in values of $10^{13}$ cm$^{-2}$. Blue (red) dashed lines indicate quadratic (linear) fits to the data.

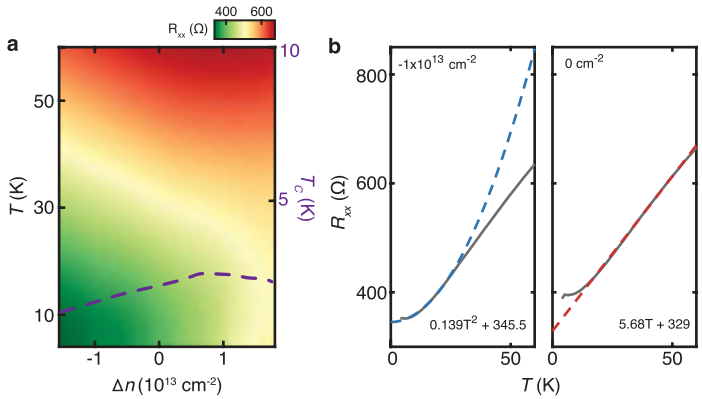


**Extended Data Fig. 3 | T-linear behaviour observed in D3. a**, Colour plot of resistance vs temperature and doping. Doping dependent superconducting critical temperature (from Extended Data Fig. 2) is superimposed on the colour plot. **b**, $R_{xx}$ versus temperature for various dopings. Blue (red) dashed lines indicate quadratic (linear) fits to the data.